



ETIN-MIP

Extratropical-Tropical Interaction Model Intercomparison Project – Protocol and Initial Results

Sarah M. Kang^{1*}, Matt Hawcroft^{2,3}, Baoqiang Xiang^{4,5}, Yen-Ting Hwang⁶,
Gabriel Cazes⁷, Francis Codron⁸, Traute Crueger⁹, Clara Deser¹⁰, Øivind Hodnebrog¹¹,
Hanjun Kim¹, Jiyeong Kim¹, Yu Kosaka¹², Teresa Losada¹³, Carlos R. Mechoso¹⁴,
Gunnar Myhre¹¹, Øyvind Seland¹⁵, Bjorn Stevens⁹, Masahiro Watanabe¹⁶, Sungduk Yu¹⁷

¹Ulsan National Institute of Science and Technology, Ulsan, Republic of Korea

²University of Exeter, Exeter, United Kingdom

³University of Southern Queensland, Toowoomba, Australia

⁴NOAA/Geophysical Fluid Dynamics Laboratory, Princeton, New Jersey, USA

⁵University Corporation for Atmospheric Research, Boulder, Colorado, USA

⁶Department of Atmospheric Sciences, National Taiwan University, Taipei, Taiwan

⁸LOCEAN/IPSL, Sorbonne Université, CNRS, IRD, MNHN, Paris, France

⁹Max Planck Institute for Meteorology, Hamburg, Germany

¹⁰Climate and Global Dynamics, National Center for Atmospheric Research, Boulder, Colorado,
USA

¹¹Center for International Climate Research (CICERO), Oslo, Norway

¹²Research Center for Advanced Science and Technology, The University of Tokyo, Tokyo,
Japan

¹³Universidad Complutense de Madrid, Madrid, Spain

¹⁴Department of Atmospheric and Oceanic Sciences, University of California, Los Angeles,
California, USA

¹⁵Norwegian Meteorological Institute, P.O. Box 43, Blindern, 0313 Oslo, Norway

¹⁶Atmosphere and Ocean Research Institute (AORI), The University of Tokyo, Tokyo, Japan

¹⁷Department of Geology and Geophysics, Yale University, New Haven, Connecticut, USA

*Corresponding author: Sarah M. Kang, School of Urban and Environmental Engineering, Ulsan National Institute of Science and Technology, UNIST-gil 50, Ulsan 44919, Republic of Korea.
E-mail: skang@unist.ac.kr

Early Online Release: This preliminary version has been accepted for publication in *Bulletin of the American Meteorological Society*, may be fully cited, and has been assigned DOI 10.1175/BAMS-D-18-0301.1. The final typeset copyedited article will replace the EOR at the above DOI when it is published.

1 **Abstract**

2 This article introduces the Extratropical-Tropical Interaction Model Intercomparison Project
3 (ETIN-MIP), where a set of fully coupled model experiments are designed to examine the
4 sources of longstanding tropical precipitation biases in climate models. In particular, we reduce
5 insolation over three targeted latitudinal bands of persistent model biases: the southern
6 extratropics, the southern tropics and the northern extratropics. To address the effect of regional
7 energy bias corrections on the mean distribution of tropical precipitation, such as the double-
8 Intertropical Convergence Zone problem, we evaluate the quasi-equilibrium response of the
9 climate system corresponding to a 50-year period after the 100 years of prescribed energy
10 perturbation. Initial results show that, despite a large inter-model spread in each perturbation
11 experiment due to differences in ocean heat uptake response and climate feedbacks across
12 models, the southern tropics is most efficient at driving a meridional shift of tropical
13 precipitation. In contrast, the extratropical energy perturbations are effectively damped by
14 anomalous heat uptake over the subpolar oceans, thereby inducing a smaller meridional shift of
15 tropical precipitation compared with the tropical energy perturbations. The ETIN-MIP
16 experiments allow us to investigate the global implications of regional energy bias corrections,
17 providing a route to guide the practice of model development, with implications for
18 understanding dynamical responses to anthropogenic climate change and geoengineering.

19

20

21

22

23

24 **Capsule**

25 ETIN-MIP is a community-wide effort to improve dynamical understanding of the linkages
26 between tropical precipitation and radiative biases in various regions, with implications for
27 anthropogenic climate change and geoengineering.

28

29 **Text**

30 The inter-tropical convergence zone (ITCZ) is a narrow equatorial band of intense
31 rainfall that receives one third of the global precipitation. Even a minor shift in the ITCZ position
32 is of great societal relevance not only because billions of people depend on this water source for
33 their freshwater and food production but also because the latent heat released by condensation of
34 water vapor in the atmosphere associated with tropical precipitation drives profound global
35 impacts via poleward propagating Rossby waves (Hoskins and Karoly 1981). Moreover, a
36 displacement in the ITCZ position exerts a considerable influence on the extratropics through
37 changes in the frequency of tropical cyclones (Dunstone et al. 2013; Merlis et al. 2013), the
38 poleward edge of the Hadley circulation (Kang and Lu 2012; Chemke and Polvani 2018), and the
39 midlatitude jet position (Ceppi et al. 2013; Cvijanovic et al. 2013). It is for these reasons that the
40 question of what controls the position, strength and variability of the tropical rainbelts has
41 emerged as one of the central questions of climate science (Bony et al. 2015).

42 Despite the crucial importance of correctly simulating the distribution of tropical
43 precipitation, generations of global climate models (GCMs) have had difficulty simulating the
44 observed pattern of tropical precipitation, with a too pronounced ‘double ITCZ’ (Mechoso et al.
45 1995; Zhang et al. 2015) being a robust bias. Great effort has been made to correct this bias
46 because it substantially influences the reliability of future climate projections (Zhou and Xie

47 2015). This bias manifests in both hemispherically symmetric and antisymmetric components
48 (Adam et al. 2016): the symmetric component is characterized by deficient precipitation in the
49 equatorial region and excessive precipitation in the off-equatorial region; the antisymmetric
50 component is characterized by an overestimation of precipitation in the southern tropics relative
51 to the northern tropics manifested in a too zonally oriented and eastward extended South Pacific
52 Convergence Zone (SPCZ). In this study, we will refer to the hemispherically antisymmetric
53 component as the double ITCZ bias. In general, the double ITCZ bias has been attributed to local
54 origins such as poor representation of tropical ocean-atmosphere feedbacks (Lin 2007),
55 stratocumulus clouds (Ma et al. 1996) and associated bias in tropical radiative fluxes from
56 atmospheric models (Xiang et al. 2017), unrealistic representation of convective entrainment rate
57 (Hirota et al. 2011), biased sea surface temperature (SST) thresholds leading to the erroneous
58 onset of deep convection (Belluci et al. 2010), and unrealistic winds in the eastern Pacific and
59 coastal areas (De Szoeke and Xie 2008; Zheng et al. 2011). In a recent paper, Song and Zhang
60 (2018) report on a major reduction of the double ITCZ bias in their model with a revised
61 parameterization of deep convection.

62 On the other hand, extratropical energy biases have also been proposed as a possible
63 cause of the double ITCZ bias. In particular, the warm bias in the Southern Hemisphere
64 extratropics, observed in many GCMs associated with cloud biases over the Southern Ocean, is
65 suggested to contribute to the double ITCZ bias (Hwang and Frierson 2013). In response to the
66 hemispheric energy imbalance associated with a warmer Southern Hemisphere, the Hadley
67 circulation adjusts in a way to transport energy northward via its upper branch while transporting
68 moisture southward via its lower branch (Kang et al. 2008), thereby potentially driving the
69 double ITCZ. This energetics framework, which relates the ITCZ response to the energy

70 transport by the Hadley circulation, has been successfully invoked in a number of studies to
71 explain how the ITCZ responds to extratropical thermal forcing in global climate models that do
72 not include ocean dynamics (e.g., Broccoli et al. 2006; Kang et al. 2009). Slab ocean coupled
73 GCM experiments even suggest the extratropics as the forcing location most effective at shifting
74 the ITCZ position (Seo et al. 2014), lending credibility to the hypothesis that remote effects of
75 the Southern Ocean warm bias are major contributors to the double ITCZ bias.

76 To investigate this hypothesis, several recent studies perturbed the Southern Hemisphere
77 extratropics in fully coupled atmosphere-ocean models. Kay et al. (2016) enhance cloud
78 brightness over the Southern Ocean, which is shown to result in little shift in tropical
79 precipitation, in contrast to the expectation based on slab ocean model studies. Similarly,
80 Hawcroft et al. (2016) apply targeted albedo corrections in the Southern Ocean and the double-
81 ITCZ problem persists. Mechoso et al. (2016) artificially reduce insolation over the southern
82 extratropics in two independent models. The one that more realistically simulates the sensitivity
83 of stratocumulus to underlying SST shows some improvement in the double ITCZ bias, though
84 only partially in the zonal mean. Xiang et al. (2018) contrast the tropical precipitation response
85 to increased insolation over the southern extratropics and the southern tropics respectively.
86 While the southern tropical forcing is certainly more effective at shifting the ITCZ, the extent of
87 the ITCZ shift in response to the southern extratropical forcing is still more significant than in
88 other aforementioned studies. The same conclusion is drawn from the experiments where
89 stratospheric aerosols that reflect incoming radiation are imposed in defined latitude bands
90 (Hawcroft et al. 2018). In sum, the ITCZ shift responses to extratropical energy perturbations are
91 only modest in dynamic ocean coupled GCMs, though with substantial differences among
92 models.

93 The damped ITCZ response in fully coupled simulations relative to slab ocean
94 simulations is because energy perturbations need not be balanced by the atmosphere alone but
95 are also mediated by changes in oceanic heat transport. The less the energy perturbations are
96 balanced by changes in atmospheric heat transport, due to oceanic compensation, the smaller the
97 ITCZ shift response. Previous studies indicate a wide range of the atmospheric fractional
98 contribution to the total cross-equatorial energy transport response to the Southern Hemisphere
99 extratropical cooling that spans between 20 % (Kay et al. 2016) and 62 % (Hawcroft et al. 2018).
100 Such differences may stem from differences in experimental design, different model physics, or
101 underlying biases in any given model. To address this issue, Kang et al. (2018a) suggest that
102 multimodel comparisons should be constructed to cleanly examine the nature and the spread of
103 model response to prescribed energy perturbations at different latitude bands.

104 This proposal has resulted in the Extratropical-Tropical Interaction Model
105 Intercomparison Project, or ETIN-MIP. The Green's function approach would be ideal for
106 thoroughly assessing the global impact of regional energy perturbations, and was adopted in
107 either an AMIP-type prescribed SST setting (Zhou et al. 2017) or a slab ocean setting (Liu et al.
108 2018) where warming or cooling is added over a limited domain throughout the entire globe.
109 However, this is prohibitive in practice for fully coupled models due to the high computational
110 cost. As an alternative approach, ETIN-MIP proposes to selectively perturb three target regions
111 of persistent model biases in fully coupled models. Previous studies have adopted a similar
112 approach, but used one fully coupled climate model (e.g., Hawcroft et al. 2018; Xiang et al.
113 2018; White et al. 2018). ETIN-MIP will cast light on which regions are particularly important
114 and sensitive to energy perturbations/biases in the context of their teleconnections and whether

115 this sensitivity is robust by investigating causes of inter-model diversity and the specific
116 processes that govern any spread in the models' response.

117 Numerical experiments defined by ETIN-MIP are guided by four core science questions:

- 118 • How sensitive is the partitioning of energy transport response between the atmosphere
119 and ocean to the region of forcing?
- 120 • Does the ocean heat transport response primarily result from dynamic ocean circulation
121 changes or ocean temperature anomalies?
- 122 • Which part of the ocean circulation (i.e., Ekman transport, subtropical gyres, deep
123 overturning circulation) is most effective at inducing cross-equatorial energy transport?
- 124 • How much does the inter-model response spread vary with forcing location and what are
125 the implications for understanding (a) the causes of bias in the climatology of those
126 models and (b) the likely fidelity of their future projections, individually and
127 collectively?

128 By answering these questions ETIN-MIP aims to provide an improved understanding of the link
129 between tropical precipitation and regional energy anomalies that are both local and remote.
130 Moreover, ETIN-MIP will provide a platform to study the causes of climatological biases in
131 coupled models at a process level, and the plausibility of model responses to external
132 perturbations, thereby contributing to improve our ability to make robust future projections of
133 regional patterns of climate change.

134

135 **Experimental Design**

136 The first tier of ETIN-MIP asks modeling groups to perform one control and three perturbation
137 experiments with their state-of-the-art fully coupled models. The control experiment (CNTL) is a

138 fully spun-up preindustrial run where 150 simulated years of output is requested to be provided
139 from a start date chosen to initialize subsequent perturbation experiments. The three perturbation
140 experiments are also integrated for 150 years after an abrupt reduction of solar flux over three
141 different latitude bands: the southern extratropics between 45°S-65°S (SEXT), the southern
142 tropics between 5°S-25°S (STRO), and the northern extratropics between 45°N-65°N (NEXT).
143 The geographical distribution of solar flux perturbations in all experiments are shown in Fig. 1.
144 The forcing domains correspond to regions with the largest inter-model spread in cloud radiative
145 effects (Boucher et al. 2013; Hwang and Frierson 2013). The forcing induced by the altered solar
146 flux is time varying due to the seasonal and diurnal cycles of insolation. The annual-mean of net
147 top-of-atmosphere (TOA) radiative forcing integrated over the forcing domain is constrained to
148 produce a total energy perturbation of approximately 0.8 PW, equivalent to 1.6 Wm^{-2} in the
149 global-mean.

150 In a fully coupled system, the magnitude of the imposed forcing is difficult to estimate
151 due to the slowly evolving SST and the associated feedbacks (Myhre et al. 2013). Furthermore,
152 Forster et al. (2016) demonstrates that the effective radiative forcing diagnosed from fixed SST
153 simulations is more accurate than that based on the regression method (Gregory et al. 2004).
154 Therefore, we estimate the forcing magnitude based on model experiments with fixed SSTs
155 using the GFDL AM4 (Zhao et al. 2018). AM4 integrated with the observed SST and sea ice
156 concentration is perturbed by reducing solar flux as in one of the perturbation experiments. The
157 difference of annual-mean TOA net shortwave radiation over the forcing domain between the
158 control and perturbation experiments is set to be approximately 0.8 PW in GFDL AM4. Because
159 of the inter-model differences in climatology of planetary albedo, the same perturbation in solar
160 flux does not necessarily guarantee a forcing of same magnitude. Thus, we compute a weighting

161 factor for each model experiment so as to adjust the prescribed solar flux perturbation multiplied
162 by one minus the planetary albedo in CNTL of each model to 0.8 PW (Table S1). This weighting
163 factor, which ranges between 0.80 and 1.13 depending on the forcing region and a model, is
164 applied to any diagnostics in post processing prior to taking the multi-model mean. Keeping in
165 mind that our original motivation is to address the double ITCZ bias in the mean state, we
166 analyze the last 50 year mean of 150-year integrations of coupled model experiments because 1)
167 the simulations reach a new quasi-equilibrium state after ~40 years based on the global
168 imbalance of TOA radiation as well as net surface fluxes (Fig. S1) and 2) 50 years is a long
169 enough period to remove any signatures of decadal variability. Although the deep ocean would
170 be far from reaching an equilibrium (Fig. S2), we note that it is not critical for our purpose.

171 Additional Tier 2 experiments are under development by a subset of models to further 1)
172 examine sensitivity to the type of forcing (surface vs TOA), 2) enable direct comparison between
173 fully coupled and slab ocean simulations, 3) examine linearity to forcing magnitude, 4) examine
174 the asymmetric response to cooling and heating cases, and 5) separate rapid adjustments from
175 feedback responses via fixed SST/sea ice experiments. These additional experiments will help to
176 elaborate upon and evaluate the robustness of our findings. Any modeling groups interested in
177 participating in either Tier 1 or 2 are welcome to contact the corresponding author.

178 Given the focus of ETIN-MIP on energy budgets, the diagnostics required to compute
179 meridional eddy heat and momentum fluxes for atmosphere and ocean are requested (see Table
180 S2 for descriptions). For ocean meridional mass and heat transport diagnostics, all parameterized
181 components and meridional diffusion need to be provided. The variables in Table S2 need to be
182 calculated at every time step before performing any time averages. We request to output those

183 variables at model levels (before interpolating to standard pressure levels) to better close the
184 budget.

185 ETIN-MIP model output is provided in the standardized format taken from a subset of the
186 CMIP5 output protocol. The time-mean over the last 50 years of a subset of output can be
187 obtained at <https://zenodo.org/record/3362615#.XU6585MzbOQ>. A complete set of output,
188 which is provided as (1) decadal means of each month for the entire simulation period, and (2)
189 monthly means for the first and last twenty years of the simulation period, will be made available
190 to the research community upon request to the corresponding author. Nine models participating
191 in ETIN-MIP and their descriptions are in Table 1.

192

193 **TOA Energy Perturbation and Climate Response**

194 An initial finding from ETIN-MIP is that among the three forcing domains, the southern tropics
195 is most efficient at driving a meridional shift and manipulating the equatorial peak of tropical
196 precipitation (Fig. 2, left). The two extratropical forcing cases exhibit a clear meridional shift of
197 tropical precipitation in the Atlantic and Indian Ocean, while a common equatorially
198 concentrated drying response appears in the Pacific. The off-equatorial response in the Pacific
199 features a meridional shift in NEXT while it is nearly symmetric in SEXT. To quantify these
200 effects, we use the tropical precipitation asymmetry index (P_{ASY}), introduced by Hwang and
201 Frierson (2013), and the equatorially symmetric precipitation index (P_{SYM}), introduced by Adam
202 et al. (2016): P_{ASY} , the difference in the precipitation averaged between 0-20°N and that between
203 0-20°S normalized by the mean precipitation between 20°S-20°N, measures the meridional shift,
204 while P_{SYM} , the average precipitation over 2°S-2°N divided by that over 20°S-20°N minus 1
205 measures the relative magnitude of the equatorial peak. Changes in P_{ASY} and P_{SYM} as well as

206 changes in total precipitation between 20°S-20°N are shown in Fig. 3. For reference, overlaid
207 with CNTL as a gray star symbol is the observed value based on Global Precipitation
208 Climatology Project (GPCP) data averaged between 1980 and 1999. The results clearly show
209 that the imprint of TOA energy biases on tropical precipitation differs depending on the
210 geographic location of the bias.

211 Figure 4 shows the global surface temperature response to the prescribed TOA cooling in
212 the three perturbation experiments. The local cooling response over the forcing domain is most
213 pronounced in NEXT (-4.00 K) while the forcing domains are cooled significantly less in the
214 other two experiments with -1.92 in SEXT and -0.89 in STRO. Although STRO exhibits only a
215 weak inter-hemispheric contrast in the surface temperature response (Fig. 4, left), it exhibits the
216 largest meridional gradient of SST anomalies within 20°S and 20°N (Fig. 2, right).

217 Consequently, STRO induces the strongest cross-equatorial Hadley circulation anomalies (Fig. 4,
218 right) and the largest meridional shift of tropical precipitation (Fig. 2, left). Figure 5a shows that
219 the inter-hemispheric difference of tropical SST response is positively correlated with P_{ASY}
220 response. When all model experiments are considered, 85 % of the inter-model variance of P_{ASY}
221 response is explained by variations in the meridional gradient of tropical SST anomalies. The
222 variance of P_{ASY} response is nearly as well correlated with the cross-equatorial atmospheric
223 energy transport anomalies (F_{ATM0}), even within each experiment (Fig. 5b). This suggests that
224 the ITCZ shift, atmospheric energy transport and tropical SST changes are strongly coupled with
225 each other. Given this, we proceed to explain the inter-model spread of P_{ASY} response by
226 investigating the cause of the inter-model spread of F_{ATM0} through examining the atmospheric
227 energy budget.

228

229 **Tropical Precipitation Response and Atmospheric Energy Budget**

230 The extent to which the TOA energy perturbations induce a meridional shift of tropical
231 precipitation is controlled by processes that determine the atmospheric energy budget in an
232 equilibrium state:

$$233 \quad E_{\text{TOA}} - E_{\text{OCN}} = \nabla \cdot F_{\text{ATM}} \quad (1)$$

234 where all quantities indicate the climatological difference between the perturbed and CNTL
235 experiments. Note that the atmospheric energy storage can be neglected when diagnosing the
236 quasi-equilibrated annual-mean response. E_{TOA} is the anomalous net downward radiation at
237 TOA, E_{OCN} is the anomalous net downward surface energy flux, and F_{ATM} is the anomalous
238 northward atmospheric energy transport. Eq. (1) states that net atmospheric column energy input
239 through the TOA and ocean surface is balanced by a divergence of atmospheric energy transport.

240 The anomalous net downward radiation at TOA, E_{TOA} includes the prescribed forcing,
241 which is the fraction of solar flux perturbation ΔS felt by the system, $E_S \equiv (1 - \alpha)\Delta S$ where α is
242 the climatological mean planetary albedo in CNTL. As mentioned earlier, the magnitude of
243 prescribed forcing across models may differ due to model differences in α , thus, the weighting
244 factor in Table S1 is accounted for to adjust the forcing magnitude to 0.8 PW in all models. The
245 difference between E_{TOA} and the prescribed forcing is referred to as the TOA response (denoted
246 as $E_{\text{TOA-S}}$), which takes into account both rapid adjustments, which modify the radiative budget
247 indirectly through fast atmospheric and surface changes, and feedbacks, which operate through
248 changes in climate variables that are mediated by surface temperature changes (Sherwood et al.
249 2015). The anomalous net surface energy flux E_{OCN} represents heat uptake by the ocean, which
250 involves both ocean heat storage and ocean heat transport divergence (Liu et al. 2018). In a slab
251 ocean setting where SSTs are computed based on the local surface energy budget while

252 neglecting ocean dynamics, the net surface energy flux response E_{OCN} is zero by construction. In
253 a fully coupled setting, the net surface energy flux response E_{OCN} can be shaped by distinct
254 oceanic processes that take place on different time scales. Within the first decade, Ekman
255 transport arising from the coupling between the Hadley circulation and the oceanic subtropical
256 cells as well as gyre circulations formed by the surface wind patterns are primarily responsible
257 for ocean heat uptake changes E_{OCN} (Fig. S3). Slow ocean processes associated with deep
258 overturning circulation also play an important role in altering E_{OCN} , but the adjustment time
259 scale varies considerably depending on the forcing region. For example, the Atlantic Meridional
260 Overturning Circulation (AMOC) strength adjusts after approximately 50 years in NEXT while it
261 steadily increases for the entire simulation period of 150 years in SEXT (Fig. S2). In addition to
262 versions of oceanic circulations, the prescribed forcing may also influence the ocean heat uptake
263 response E_{OCN} and the associated SST pattern via anomalous advection by the mean circulation,
264 which is a process on decadal time scales (Li et al. 2013; Wang et al. 2018). That is, during the
265 last 50-year period that we analyze here, multiple ocean processes play a role in shaping E_{OCN} .
266 Attribution of E_{OCN} to different oceanic processes is a challenging topic to be further explored.

267 To obtain an equation for the cross-equatorial atmospheric energy transport anomalies
268 F_{ATM0} , which is shown to be strongly correlated with the ITCZ shift (Fig. 5b), we reformulate
269 Eq. (1) to depict the hemispheric asymmetry by spatially integrating over the Southern
270 Hemisphere with the global-mean removed:

$$271 \quad \langle E_S \rangle = -\langle E_{\text{TOA-S}} \rangle + \langle E_{\text{OCN}} \rangle + F_{\text{ATM0}} \quad (2)$$

272 where brackets denote the spatial integral of the anomaly from the global-mean over the
273 Southern Hemisphere. All variables have the units in Watt. Eq. (2) indicates that the hemispheric
274 asymmetry in prescribed forcing $\langle E_S \rangle$ is balanced by adjusting the hemispheric asymmetry in

275 TOA radiation response $\langle E_{\text{TOA-S}} \rangle$ and ocean heat uptake response $\langle E_{\text{OCN}} \rangle$, and the cross-
276 equatorial atmospheric energy transport response F_{ATM0} (Fig. 6a). We define the fraction of
277 prescribed forcing balanced by each component as the TOA compensation, oceanic
278 compensation, and atmospheric compensation:

$$279 \quad C_{\text{TOA}} \equiv \frac{-\langle E_{\text{TOA-S}} \rangle}{\langle E_{\text{S}} \rangle}, C_{\text{OCN}} \equiv \frac{\langle E_{\text{OCN}} \rangle}{\langle E_{\text{S}} \rangle}, \text{ and } C_{\text{ATM}} \equiv \frac{F_{\text{ATM0}}}{\langle E_{\text{S}} \rangle}$$

280 such that $C_{\text{TOA}} + C_{\text{OCN}} + C_{\text{ATM}} = 1$.

281 Figure 7 compares the fractional compensation by each component in all model
282 experiments. Consistent with the sensitivity of P_{ASY} response to the location of forcing domains,
283 all models exhibit the largest C_{ATM} in STRO associated with the smallest C_{OCN} . This implies that
284 radiation biases over the tropics are more effective in driving the spurious double ITCZ problem
285 in current climate models than extratropical radiation biases (Hawcroft et al. 2018; Xiang et al.
286 2017; Xiang et al. 2018; Green et al. 2019). A relatively smaller C_{ATM} for the extratropical
287 experiments is associated with a larger C_{OCN} while the contribution from radiative adjustment
288 (C_{TOA}) is small and highly uncertain in terms of sign. Comparing the two extratropical
289 experiments, NEXT induces a slightly larger C_{ATM} than SEXT in the multi-model mean,
290 consistent with a stronger cross-equatorial Hadley circulation in NEXT (Fig. 4, right). However,
291 this sensitivity to the forced hemisphere is model dependent, with 3 out of 9 models exhibiting
292 the opposite sensitivity with a larger C_{ATM} in SEXT. The causes of these differences are a topic
293 of planned future research within ETIN-MIP.

294 Recent studies attribute the muted tropical precipitation responses to extratropical energy
295 perturbations in fully coupled models to oceanic processes (Deser et al. 2015; Kay et al. 2017;
296 Green and Marshall 2017). The oceanic compensation C_{OCN} is zero in a slab ocean setting by
297 construction, hence, a larger fraction of energy perturbations must be balanced by the

298 atmospheric energy transport compared to the case when coupled to a full ocean model. Some
299 studies point to the coupling between the Hadley circulation and the oceanic subtropical cells for
300 the reduced tropical precipitation responses (Green and Marshall 2017; Schneider 2017; Kang et
301 al. 2018a; Green et al. 2019). Ekman coupling ensures that the Hadley circulation and the
302 oceanic subtropical cells transport the anomalous energy in the same direction, thereby damping
303 the ITCZ response. If Ekman coupling is the primary factor in the oceanic damping effect, STRO
304 is expected to exhibit the largest oceanic compensation C_{OCN} considering that the anomalous
305 Hadley cell strength is by far strongest (Fig. 4, right), yet STRO exhibits the smallest C_{OCN} (Fig.
306 7). The Ekman damping effect by the oceanic subtropical cells should be included in the fraction
307 of C_{OCN} resulting from the ocean heat uptake response within the tropics. Red bars in Fig. 7
308 display the tropical component of C_{OCN} , computed by taking into account E_{OCN} between 30°S
309 and 30°N in isolation. The tropical C_{OCN} in STRO is smaller than that in NEXT by 48 % despite
310 a significantly stronger anomalous Hadley circulation in STRO (Fig. 4, right). In addition, STRO
311 and SEXT exhibit a comparable tropical C_{OCN} despite a stark contrast in the anomalous Hadley
312 cell strength. The result not only implicates other potentially important oceanic damping
313 pathways than the Ekman transport but also suggests a limited ability of the ocean's Ekman
314 transport to compensate the energy perturbations, potentially due to small gross stability in the
315 shallow ocean mixed layer (Kang et al. 2018b).

316 A question then arises as to which oceanic processes are responsible for modulating the
317 oceanic compensation. Figure 8 shows that E_{OCN} in NEXT primarily occurs in the subpolar
318 North Atlantic and along the western boundary currents while that in SEXT primarily occurs in
319 the Southern Ocean. Indeed, the full C_{OCN} in the extratropical experiments is dominated by the
320 extratropical component (Fig. 7). In other words, it is the extratropical oceanic processes that

321 boost the oceanic compensation in the extratropical experiments, thereby shaping the overall
322 sensitivity of C_{OCN} to forcing region (Yu and Pritchard 2019). To examine the origin of E_{OCN} ,
323 Figure 9 compares the anomalous ocean meridional overturning circulation (MOC)
324 streamfunction and the mean ocean temperature in CNTL on the left column with the anomalous
325 ocean temperature and the mean ocean MOC streamfunction in CNTL on the right column. The
326 left column allows an estimation of the ocean heat transport change resulting from ocean
327 circulation changes (i.e., the dynamic term) while the right column allows an estimation of that
328 resulting from ocean temperature changes (i.e., the thermodynamic term). In NEXT, the subpolar
329 North Atlantic E_{OCN} results from the dynamic term associated with a strengthened AMOC (Fig.
330 9a) while the Southern Ocean E_{OCN} in SEXT results from the thermodynamic term associated
331 with the mean upward motion at 50-60°S (Fig. 9f) (Bryan et al. 1988; Armour et al. 2016; Frey
332 et al. 2017; Xiang et al. 2018). This local ocean heat uptake response E_{OCN} over the forced
333 latitude band is larger in SEXT than in NEXT for all models, by a factor of 1.64 in the multi-
334 model mean (Fig. 8, left). However, remote oceanic processes outside of the forcing region as
335 well as its interaction with radiative feedbacks add uncertainty to the sensitivity of C_{OCN} , with it
336 being larger in SEXT for only two thirds of the models and a third exhibiting the opposite
337 sensitivity (Fig. 7). In STRO, an anomalously anticlockwise circulation in the southern tropical
338 upper ocean (Fig. 9b) gives rise to a southward ocean heat transport which is largely cancelled
339 by the thermodynamic term associated with the subsurface warming driven by the anomalous
340 downwelling (Fig. 9e). As a result, the equatorial C_{OCN} in STRO is small relative to the
341 extratropical cases (Fig. 7) (Xiang et al. 2018; Hawcroft et al. 2018). The ETIN-MIP output will
342 allow a rigorous decomposition of the anomalous ocean heat transport into the thermodynamic
343 and dynamic terms.

344 The TOA compensation C_{TOA} is highly uncertain for all experiments, resulting in a near-
345 zero C_{TOA} in the multi-model mean with a large inter-model spread (Fig. 7). A large diversity in
346 C_{TOA} originates from multiple factors such as rapid adjustment and climate feedbacks associated
347 with clouds, water vapor, surface albedo and Planck response. For the purpose of separating the
348 contribution of rapid adjustment to the diversity of C_{TOA} from contribution of climate feedbacks,
349 we plan to perform fixed SST/sea ice experiments for Tier 2. Potential factors responsible for the
350 large inter-model spread of C_{TOA} is the uncertainty in sea ice and cloud responses. Since the ice-
351 albedo feedback and shortwave low-cloud feedback become weak during the winter months, we
352 weight the monthly changes in sea ice and low cloud cover by monthly insolation before taking
353 the annual mean in Fig. 10. In NEXT, HadGEM2-ES exhibits the largest increase in sea ice
354 cover over the northern high latitudes (Fig. 10a), which greatly amplifies the forcing effect, so
355 that the radiative adjustment acts as a positive feedback rather than a compensating effect (i.e.,
356 $C_{\text{TOA}} < 0$) (Fig. 7). In the extratropical cases, the low cloud cover tends to increase within and
357 equatorward of the forced latitude band (Figs. 10d and 10f), due to an increase in lower
358 tropospheric stability associated with a cooler boundary layer (Wood and Bretherton 2006). In
359 SEXT, NCAR CESM exhibits the largest low cloud cover increase in the southern subtropics to
360 mid-latitudes, which enhances the reflected shortwave radiation thereby amplifying the forcing
361 effect, while MPI-ESM1.2 exhibits the smallest changes in low cloud cover. This is consistent
362 with negative C_{TOA} in NCAR CESM and positive in MPI-ESM1.2 (Fig. 7). HadGEM2-ES in
363 SEXT exhibits a hemispherically symmetric response in both sea ice and low cloud cover
364 relative to other models (Fig. 10c and 10f), so that the radiative compensation C_{TOA} is nearly
365 zero (Fig. 7). An ETIN-MIP study under development will apply the approximate partial
366 radiative perturbation method (Taylor et al. 2007) and kernel method (Pendergrass et al. 2018) to

367 investigate the cause of inter-model diversity of TOA compensation and its dependence on
368 forcing location.

369

370 **Broader Implications**

371 A primary motivation for ETIN-MIP is to identify the remote energy biases that are potentially
372 important for causing the double ITCZ bias. Understanding how regional energy perturbations
373 affect the tropical precipitation pattern is of fundamental importance for improving not only the
374 present-day double ITCZ bias in many current climate models but also the accuracy of
375 projections of future changes in tropical precipitation due to the uneven regional distribution of
376 warming (e.g., Arctic amplification, Serreze and Barry 2011; Screen et al. 2018).

377 Applying a forcing over finite latitudinal bands in a coupled model framework, similar to
378 the ETIN-MIP experiment configuration, has proven to be useful for determining the causes of
379 climate change patterns (Stuecker et al. 2018). We envision ETIN-MIP can be generalized to
380 study other aspects of the climate response beyond tropical precipitation. Firstly, understanding
381 how the spatial pattern of tropical Pacific SST evolves within ETIN-MIP will provide insights
382 relevant for a current topic of controversy - whether the equatorial Pacific under global warming
383 would warm more in the east than the west (i.e., El Niño-like) or the reverse (e.g., Kohyama et
384 al. 2017). Secondly, we plan to investigate how regional energy perturbations/biases influence
385 the major climate modes such as the El Niño-Southern Oscillation (e.g., Timmermann et al.
386 2007), which will help understand their future projections under radiative forcing with complex
387 spatial patterns. Thirdly, ETIN-MIP data is suitable for exploring one of the intriguing
388 unanswered questions about Earth's albedo: the hemispheric symmetry in planetary albedo
389 despite a substantial hemispheric asymmetry in clear-sky albedo (Voigt et al. 2013).

390 Furthermore, ETIN-MIP experiments can be examined within the context of geoengineering
391 where injecting stratospheric sulfate aerosols is proposed as a potential means of deliberately
392 offsetting the global warming effect (Crutzen 2006; Jones et al. 2017). For example, ETIN-MIP
393 results may highlight regions where geoengineering techniques may be applied for specific
394 climate change mitigation effects to be maximized. Thus, the project encourages the wider
395 research community to use the ETIN-MIP dataset for evaluating and understanding the global
396 manifestation of regional energy perturbations, which can be viewed as energetics biases,
397 anthropogenic forcings, or geoengineering applications.

398

399 **Summary**

400 In ETIN-MIP, 9 climate modeling groups have performed common numerical experiments
401 aimed at enhancing our understanding of the mechanisms for two-way extratropics-tropics
402 interactions. The link between the extratropics and tropics is of high societal concern given its
403 role in controlling regional patterns of climate change. Improving our understanding of the
404 mechanisms that enable these connections would significantly enhance our ability to predict and
405 prepare for future changes in regional hydrology. The spirit of ETIN-MIP is strongly in line with
406 one of the four questions of the World Climate Research Programme's Grand Challenge on
407 Clouds, Circulation and Climate Sensitivity (Bony et al. 2015).

408 In keeping with the original motivation for ETIN-MIP, namely to provide guidance on
409 identifying the origin of the double ITCZ bias, we have presented initial results focused on
410 tropical precipitation and energetics. The results have practical implications for GCM
411 development strategy and suggest that fixing tropical biases would be a more viable option for
412 alleviating hemispherically antisymmetric components of tropical precipitation biases while

413 fixing extratropical biases is more desirable for improving the hemispherically symmetric
414 component of tropical precipitation biases. It also implies that the ability of extratropical biases
415 to manifest the hemispherically antisymmetric component of the double ITCZ bias would depend
416 on the strength of stratocumulus-SST feedback in the subtropics (Mechoso et al. 2016). For
417 example, the effect of extratropical biases diminishes away from the source region, but the rate
418 of damping would be weaker in models with a stronger coupling between the subtropical
419 stratocumulus and SST that acts as a positive feedback, hence, extratropical biases are able to
420 project onto the double ITCZ bias in some models. The limited ability of extratropical biases to
421 meridionally displace the tropical precipitation compared to tropical biases is due to efficient
422 heat uptake response by extratropical oceanic processes (Figs. 6 and 7). It suggests constraining
423 tropical response to regional energy perturbations requires improved understanding of deep
424 ocean circulation response. This project will enhance our understanding of the origin of
425 longstanding double ITCZ bias, which is an essential first step in informing model developers.
426 More generally, ETIN-MIP will advance our physical understanding of the atmospheric and
427 oceanic circulation responses to regional energy perturbations in a fully coupled framework, and
428 provides a resource for the climate dynamics community to understand the plausibility of
429 different model responses to such regionally varying energy perturbations, including those
430 expected from anthropogenic climate change.

431

432

433

434

435

436 **References**

- 437 Adam, O., T. Schneider, F. Brient, and T. Bischoff, 2016: Relation of the double-ITCZ bias to
438 the atmospheric energy budget in climate models: Double-ITCZ bias and atmospheric energy
439 budget. *Geophys. Res. Lett.*, **43**, 7670–7677, doi:10.1002/2016GL069465.
440
- 441 Armour, K. C., J. Marshall, J. R. Scott, A. Donohoe, and E. R. Newsom, 2016: Southern Ocean
442 warming delayed by circumpolar upwelling and equatorward transport. *Nat. Geosci.*, **9**, 549-554.
443
- 444 Bellucci, A., S. Gualdi, and A. Navarra, 2010: The Double-ITCZ Syndrome in Coupled General
445 Circulation Models: The Role of Large-Scale Vertical Circulation Regimes. *J. Climate*, **23**(5),
446 1127-1145.
447
- 448 Bony, S. and Coauthors, 2015: Clouds, circulation and climate sensitivity. *Nat. Geosci.*, **8**, 261–
449 268, doi:10.1038/ngeo2398.
450
- 451 Boucher, O., and Coauthors, 2013: Climate change 2013: The Physical Science Basis. In
452 *Contribution of Working Group I to the Fifth Assessment Report of the Intergovernmental Panel*
453 *on Climate Change* (chap. 7, 1535 pp.). Cambridge, UK and New York: Cambridge University
454 Press.
455
- 456 Broccoli, A. J., K. A. Dahl, and R. J. Stouffer, 2006: Response of the ITCZ to Northern
457 Hemisphere cooling. *Geophys. Res. Lett.*, **33**(1), L01702, doi:10.1029/2005GL024546.
458
- 459 Bryan, K., S. Manabe, and J. Spelman, 1988: Interhemispheric Asymmetry in the Transient
460 Response of a Coupled Ocean-Atmosphere Model to a CO₂ Forcing. *J. Phy. Ocn.*, **18**, 851-867.
461
- 462 Ceppi, P., Y.-T. Hwang, X. Liu, D. M. W. Frierson, and D. L. Hartmann, 2013: The relationship
463 between the ITCZ and the Southern Hemispheric eddy-driven jet. *J. Geophys. Res. Atmos.*, **118**,
464 5136–5146, doi:10.1002/jgrd.50461.
465
- 466 Chemcke R., and L. M. Polvani, 2018: Exploiting the abrupt 4xCO₂ scenario to elucidate
467 tropical expansion mechanisms. *J. Climate*,
468
- 469 Chiang, J. C., and C. M. Bitz, 2005: Influence of high latitude ice cover on the marine
470 Intertropical Convergence Zone. *Clim. Dyn.*, **25**(5), 477-496.
471
- 472 Collins, W. J., and Coauthors, 2011: Development and evaluation of an Earth-System model –
473 HadGEM2. *Geosci. Model Dev.*, **4**, 1051-1075, doi:10.5194/gmd-4-1051-2011.
474
- 475 Crutzen, P. J., 2006: Albedo enhancements by stratospheric sulfur injections: A contribution to
476 resolve a policy dilemma? *Climatic Change*, **77**, 211–219, doi:10.1007/s10584-006-9101-y.
477
- 478 Cvijanovic, I., P. L. Langen, E. Kaas, and P. D. Ditlevsen, 2013: Southward intertropical con423
479 vergence zone shifts and implications for an atmospheric bipolar seesaw. *J. Climate*, **26** (12), 424
480 4121–4137, doi:10.1175/JCLI-D-12-00279.1.

481
482 Delworth, T. L., and Coauthors, 2006: GFDL's CM2 Global Coupled Climate Models. Part I:
483 Formulation and Simulation Characteristics. *J. Climate*, **19**, 643-674.
484
485 Deser, C., R. A. Tomas, and L. Sun, 2015: The role of ocean-atmosphere coupling in the zonal-
486 mean atmospheric response to Arctic sea ice loss. *J. Climate*, **28**(6), 2168-2186.
487
488 De Szoeko, S. P., and S. P. Xie, 2008: The tropical eastern Pacific seasonal cycle: Assessment of
489 errors and mechanisms in IPCC AR4 coupled ocean - Atmosphere general circulation models. *J.*
490 *Climate*, **21**(11), 2573-2590.
491
492 Dufresne, J.-L., and Coauthors, 2013: Climate change projections using the IPSL-CM5 Earth
493 System Model: from CMIP3 to CMIP5. *Clim. Dyn.*, **40**, 2123-2165, doi:10.1007/s00382-012-
494 1636-1.
495
496 Dunstone, N., D. Smith, B. Booth, L. Hermanson, and R. Eade, 2013: Anthropogenic aerosol
497 438 forcing of atlantic tropical storms. *Nat. Geosci.*, **6**(7), 534-539, doi:10.1038/ngeo1854.
498
499 Frey, W. R., E. A. Maroon, A. G. Pendergrass, and J. E. Kay, 2017: Do Southern Ocean cloud
500 feedbacks matter for 21st century warming? *Geophys. Res. Lett.*, **44**, 12,447-12,456.
501
502 Forster, P. M., and Coauthors, 2016: Recommendations for diagnosing effective radiative forcing
503 from climate models for CMIP6. *J. Geophys. Res. Atmos.*, **121**, 12,460-12,475,
504 <https://doi.org/10.1002/2016JD025320>.
505
506 Green, B., and J. Marshall, 2017: Coupling of trade winds with ocean circulation damps ITCZ
507 shifts. *J. Climate*, **30**(12), 4395-4411.
508
509 Green, B., J. Marshall, and J.-M. Campin, 2019: The 'sticky' ITCZ: ocean-moderated ITCZ
510 shifts. *Clim. Dyn.*, **53**, 1-19.
511
512 Gregory, J. M., and Coauthors, 2004: A new method for diagnosing radiative forcing and climate
513 sensitivity. *Geophys. Res. Lett.*, **31**, L03205, doi:10.1029/2003GL018747.
514
515 Hawcroft, M., J. M. Haywood, M. Collins, A. Jones, A. C. Jones, and G. Stephens, 2016:
516 Southern Ocean albedo, inter-hemispheric energy transports and the double ITCZ: global
517 impacts of biases in a coupled model. *Clim. Dyn.*, **48**, 2279-2295.
518
519 Hawcroft, M., J. M. Haywood, M. Collins, and A. Jones, 2018: The contrasting climate response
520 to tropical and extratropical energy perturbations. *Clim. Dyn.*, 1-19, doi:10.1007/s00382-018-
521 4076-8.
522
523 Hirota, N., Y. N. Takayabu, M. Watanabe, and M. Kimoto, 2011: Precipitation Reproducibility
524 over Tropical Oceans and Its Relationship to the Double ITCZ Problem in CMIP3 and MIROC5
525 Climate Models. *J. Climate*, **24**(18), 4859-4873.
526

527 Hoskins, B. J., and D. J. Karoly, 1981: The Steady Linear Response of a Spherical Atmosphere
528 to Thermal and Orographic Forcing. *J. Atmos. Sci.*, **38**, 1179–1196.
529

530 Hurrell, J. W., and Coauthors 2013: The community earth system model: a framework for
531 collaborative research. *Bull. Am. Meteorol. Soc.*, **94**, 1339–1360.
532

533 Hwang, Y.-T., and D. M. Frierson, 2013: Link between the double-Intertropical Convergence
534 Zone problem and cloud biases over the Southern Ocean. *Proc. Nat. Aca. of Sci.*, **110**(13), 4935-
535 4940.
536

537 Jones, A. C., Haywood, J. M., Dunstone, N., Emanuel, K., Hawcroft, M. K., Hodges, K. I., &
538 Jones, A., 2017: Impacts of hemispheric solar geoengineering on tropical cyclone frequency.
539 Nature communications, **8**(1), 1382.
540

541 Kang, S. M., I. M. Held, D. M. Frierson, and M. Zhao, 2008: The response of the ITCZ to
542 extratropical thermal forcing: Idealized slab-ocean experiments with a GCM, *J. Climate*, **21**(14),
543 3521-3532.
544

545 Kang, S. M., Frierson, D. M., & Held, I. M., 2009: The tropical response to extratropical thermal
546 forcing in an idealized GCM: The importance of radiative feedbacks and convective
547 parameterization. *J. Atmos. Sci.*, **66**(9), 2812-2827.
548

549 Kang, S. M., and J. Lu, 2012: Expansion of the Hadley Cell under Global Warming: Winter
550 versus Summer. *J. Climate*, **25**, 8387–8393, doi:10.1175/JCLI-D-12-00323.1.
551

552 Kang, S. M., Y. Shin, and S. P. Xie, 2018: Extratropical forcing and tropical rainfall distribution:
553 energetics framework and ocean Ekman advection. *npj Clim. and Atm. Sci.*, **1**,
554 doi:10.1038/s41612-017-0004-6.
555

556 Kang, S. M., Y. Shin, and F. Codron, 2018: The partitioning of poleward energy transport
557 response between the atmosphere and Ekman flux to prescribed surface forcing in a simplified
558 GCM. *Geoscience Letters*, **5**, doi:10.1186/s40562-018-0124-9.
559

560 Kay, J. E., C. Wall, V. Yettella, B. Medeiros, C. Hannay, P. Caldwell, and C. Bitz, 2016: Global
561 climate impacts of fixing the Southern Ocean shortwave radiation bias in the Community Earth
562 System Model (CESM). *J. Climate*, **29**(12), 4617-4636.
563

564 Kohyama, T., D. L. Hartmann, and D. S. Battisti, 2017: La Niña–like Mean-State Response to
565 Global Warming and Potential Oceanic Roles. *J. Climate*, **30**, 4207–4225, doi:10.1175/JCLI-D-
566 16-0441.1.
567

568 Li, C., L. Wu, and S.-P. Xie, 2013: Impacts of Interhemispheric Asymmetric Thermal Forcing on
569 Tropical Pacific Climate: Surface Air–Sea Coupling and Subduction. *J. Climate*, **26**, 575–582.
570

571 Li, G., and S. P. Xie, 2014: Tropical Biases in CMIP5 Multimodel Ensemble: The Excessive
572 Equatorial Pacific Cold Tongue and Double ITCZ Problems. *J. Climate*, **27**(4), 1765-1780.

573
574 Lin, J.-L., 2007: The Double-ITCZ Problem in IPCC AR4 Coupled GCMs: Ocean–Atmosphere
575 Feedback Analysis. *J. Climate*, **20**, 4497–4525.
576
577 Liu, F., J. Lu, O. Garuba, L. R. Leung, Y. Luo, and X. Wan, 2018: Sensitivity of Surface
578 Temperature to Oceanic Forcing via q -Flux Green’s Function Experiments. Part I: Linear
579 Response Function. *J. Climate*, **31**, 3625–3641, doi:10.1175/JCLI-D-17-0462.1.
580
581 Liu, W., J. Lu, S.-P. Xie, and A. Fedorov, 2018: Southern Ocean Heat Uptake, Redistribution,
582 and Storage in a Warming Climate: The Role of Meridional Overturning Circulation. *J. Climate*,
583 **31**, 4727–4743, doi:10.1175/JCLI-D-17-0761.1.
584
585 Ma, C.-C., C. R. Mechoso, A.W. Robertson, A. Arakawa, 1996: Peruvian Stratus Clouds and the
586 Tropical Pacific Circulation: A Coupled Ocean-Atmosphere GCM Study, *J. Climate*, **9**, 1635–
587 1645.
588
589 Martin, G. M., and Coauthors, 2011: The HadGEM2 family of Met Office Unified Model
590 climate configurations, *Geosci. Model Dev.*, **4**, 723–757, doi:10.5194/gmd-4-723-2011.
591
592 Mauritsen, T., and Coauthors, 2019: Developments in the MPI-M Earth System Model version
593 1.2 (MPI-ESM1.2) and its response to increasing CO₂. *J. Adv. Model. Earth Syst.*, **11**, 998–
594 1038.
595
596 Mechoso, C. R., and Coauthors, 1995: The seasonal cycle over the tropical pacific in coupled
597 ocean–atmosphere general circulation models. *Mon. Weather Rev.*, **123**(9), 2825–2838.
598
599 Mechoso, C. R., T. Losada, S. Koseki, E. Mohino- Harris, N. Keenlyside, A. Castaño- Tierno,
600 T. A. Myers, B. Rodrigues-Fonseca, and T. Toniazzo, 2016: Can reducing the incoming energy
601 flux over the Southern Ocean in a CGCM improve its simulation of tropical climate?. *Geophys.*
602 *Res. Lett.*, **43**, 11,057–11,063, doi:10.1002/2016GL071150.
603
604 Merlis, T. M., M. Zhao, and I. M. Held, 2013: The sensitivity of hurricane frequency to ITCZ
605 changes and radiatively forced warming in aquaplanet simulations. *Geophys. Res. Lett.*, **40**,
606 4109–4114, doi:10.1002/grl.50680.
607
608 Mitchell, D., and Coauthors, 2017: Half a degree Additional warming, Projections, Prognosis
609 and Impacts (HAPPI): Background and Experimental Design, *Geosci. Model Dev.*, **10**(2), 571–
610 583.
611
612 Müller, W. A., and Coauthors, 2018: A high-resolution version of the Max Planck Institute Earth
613 System Model (MPI-ESM1.2-HR). *J. Adv. Model. Earth Syst.*, **10**, 1383–1413,
614 doi:10.1029/2017MS001217.
615
616 Myhre, G., and Coauthors, 2013: Anthropogenic and natural radiative forcing, in *Climate*
617 *Change 2013: The Physical Science Basis. Contribution of Working Group I to the Fifth*

618 *Assessment Report of the Intergovernmental Panel on Climate Change*, edited by T. F. Stocker et
619 al., pp. 659– 740, Cambridge Univ. Press, Cambridge, U. K., and New York.

620

621 Pendergrass, A. G., A. Conley, F. M. Vitt, 2018: Surface and top-of-atmosphere radiative
622 feedback kernels for CESM-CAM5. *Earth System Science Data*, **10**(1), 317-324.

623

624 Schneider, T., T. Bischoff, and G. H. Haug, G. H., 2014: Migrations and dynamics of the
625 intertropical convergence zone. *Nature*, **513**, 45-53.

626

627 Schneider, T., 2017: Feedback of Atmosphere- Ocean Coupling on Shifts of the Intertropical
628 Convergence Zone. *Geophys. Res. Lett.*, **44**(22), 11,644-11,653.

629

630 Screen, J. A., C. Deser, D. M. Smith, X. Zhang, R. Blackport, P. J. Kushner, T. Oudar, K. E.
631 McCusker and L. Sun, 2018: Consistency and causes of discrepancy in the atmospheric response
632 to Arctic sea ice loss across climate models. *Nat. Geosci.*, doi:10.1038/s41561-018-0059-y.

633

634 Seo, J., S. M. Kang, and D. M. W. Frierson, 2014: Sensitivity of intertropical convergence zone
635 movement to the latitudinal position of thermal forcing. *J. Climate*, **27**(8), 3035-3042.

636

637 Serreze, M.C. and R.G. Barry, 2011: Processes and impacts of Arctic amplification: A research
638 synthesis. *Global Planet. Change*, **77**, 85–96.

639

640 Sherwood, S. C., S. Bony, O. Boucher, C. Bretherton, P. M. Forster, J. M. Gregory, and B.
641 Stevens, 2015: Adjustments in the Forcing-Feedback Framework for Understanding Climate
642 Change. *Bull. Am. Meteorol. Soc.*, **96**, 217–228.

643

644 Song, X., and G. J. Zhang, 2018: The Roles of Convection Parameterization in the Formation of
645 Double ITCZ Syndrome in the NCAR CESM: I. Atmospheric Processes, *J. Adv. Model. Earth
646 Syst.*, **10**, 842-866.

647

648 Stuecker, M. F., and Coauthors, 2018: Polar amplification dominated by local forcing and
649 feedbacks. *Nature Climate Change*, **8**, 1076-1081, doi:10.1038/s41558-018-0339-y.

650

651 Taylor, K., and Coauthors, 2007: Estimating shortwave radiative forcing and response in climate
652 models. *J. Climate*, **20**, 2530–2543, doi:10.1175/JCLI4143.1.

653

654 Timmermann, A., and Coauthors, 2007: The Influence of a Weakening of the Atlantic
655 Meridional Overturning Circulation on ENSO. *J. Climate*, **20**, 4899–4919,
656 doi:10.1175/JCLI4283.1.

657

658 Voigt, A., B. Stevens, J. Bader, and T. Mauritsen, 2013: The Observed Hemispheric Symmetry
659 in Reflected Shortwave Irradiance. *J. Climate*, **26**, 468–477, doi:10.1175/JCLI-D-12-00132.1.

660

661 Watanabe, M., H. Shiogama, H. Tatebe, M. Hayashi, M. Ishii, and M. Kimoto, 2014:
662 Contribution of natural decadal variability to global-warming acceleration and hiatus. *Nature
663 Climate Change*, **4**, 893-897, doi:10.1038/Nclimate2355.

664
665 White, R. H., A. A. McFarlane, D. M. W. Frierson, S. M. Kang, Y. Shin, and M. Friedman,
666 2018: Tropical Precipitation and Cross-Equatorial Heat Transport in Response to Localized
667 Heating: Basin and Hemisphere Dependence. *Geophys. Res. Lett.*, **45**, 11,949–11,958,
668 doi:10.1029/2018GL078781.
669
670 Wang, K., C. Deser, L. Sun, and R. A. Tomas, 2018: Fast Response of the Tropics to an Abrupt
671 Loss of Arctic Sea Ice via Ocean Dynamics. *Geophys. Res. Lett.*, **45**, 4264–4272.
672
673 Wood, R., and C. S. Bretherton, 2006: On the Relationship between Stratiform Low Cloud Cover
674 and Lower-Tropospheric Stability. *J. Climate*, **19**, 6425–6432.
675
676 Xiang, B., M. Zhao, I. M. Held, and J.-C. Golaz, 2017: Predicting the severity of spurious
677 “double ITCZ” problem in CMIP5 coupled models from AMIP simulations. *Geophys. Res. Lett.*,
678 **44**, 1520–1527, doi: 10.1002/2016GL071992.
679
680 Xiang, B., M. Zhao, Y. Ming, W. Yu, and S. M. Kang, 2018: Contrasting Impacts of Radiative
681 Forcing in the Southern Ocean versus Southern Tropics on ITCZ Position and Energy Transport
682 in One GFDL Climate Model. *J. Climate*, **31**, 5609–5628.
683
684 Yu, S., and M. Pritchard, 2019: A strong role for the AMOC in partitioning global energy
685 transport and shifting ITCZ position in response to latitudinally discrete solar forcing in the
686 CESM1.2. *J. Climate*, **32**, 2207–2226.
687
688 Zhang, X. X., H. L. Liu, and M. H. Zhang, 2015: Double ITCZ in Coupled Ocean-Atmosphere
689 Models: From CMIP3 to CMIP5. *Geophys. Res. Lett.*, **42**(20), 8651–8659,
690 doi:10.1002/2015gl065973.
691
692 Zheng, Y. X., T. Shinoda, J. L. Lin, and G. N. Kiladis, 2011: Sea Surface Temperature Biases
693 under the Stratus Cloud Deck in the Southeast Pacific Ocean in 19 IPCC AR4 Coupled General
694 Circulation Models, *J. Climate*, **24**(15), 4139–4164, doi:10.1175/2011jcli4172.1.
695
696 Zhou, C., M. D. Zelinka, and S. A. Klein, 2017: Analyzing the dependence of global cloud
697 feedback on the spatial pattern of sea surface temperature change with a Green’s function
698 approach: ANALYZING CLOUD FEEDBACK WITH GFA. *J. Adv. Model. Earth Syst.*, **9**,
699 2174–2189, doi:10.1002/2017MS001096.
700
701 Zhou, Z.-Q., and S.-P. Xie, 2015: Effects of climatological model biases on the projection of
702 tropical climate change. *J. Climate*, **28**, 9909–9917, doi:10.1175/JCLI-D-15-0243.1
703
704
705
706

707 Table 1. Description of the nine ETIN-MIP models. The analysis of UCLA-MIT GCM is based
 708 on the average of last 20 years of 60-year integrations. The analysis of NorESM1-HAPPI for
 709 NEXT is based on the average of last 30 years of 100-year integration. The relatively insensitive
 710 climate response to time (Fig. S1) justifies the inclusion of those simulation results in our
 711 analysis.
 712

Model	Atmosphere resolution	Ocean resolution	Key reference	Note
Max Planck Institute Earth System Model (MPI-ESM1.2-LR)	T63 (1.875°×1.875°), 47 levels	MPIOM1.6.3 (1.5°), 40 levels	Mauritsen et al. (2018); Müller et al. (2018)	
Hadley Centre Global Environment Model, version 2- Earth System (HadGEM2-ES)	1.875° × 1.25°, 38 levels	1° reducing to 1/3° at equator, 40 levels	Martin et al. (2011); Collins et al. (2011)	
Norwegian Earth System Model, version 1 (NorESM1-HAPPI)	0.94°x1.25°, 26 levels	~1° and a displaced pole grid	Mitchell et al. (2017)	NEXT run for only 100 yrs
IPSL CM5A2	96x95 points, 39 levels	2° reducing to 1/2° at equator, 31 levels	Dufresne et al. (2013)	
GFDL AM4-FLOR	1°x1°, 32 levels	1°x1°, 50 levels	Xiang et al. (2018)	
GFDL CM2.1	2.5°x2°, 24 levels	1° reducing to 1/3° at equator, 50 levels	Delworth et al. (2006)	
Community Earth System Model (CESM 1.2.2)	1.9°x2.5°, 30 levels	1°(lon) and 0.6° reducing to 0.3° at equator (lat), 60 levels	Hurrell et al. (2013)	
Model for Interdisciplinary Research on Climate (MIROC5.2)	T85, 40 levels	1°x1°, 63 levels	Watanabe et al. (2014)	STRO not available
UCLA-MIT GCM	2.5°x2°, 29 levels	1°x0.3° for 10°S-10°N 1°x1° poleward 22°S/N, 46 levels	Cazes-Boezio et al. (2008)	Run for only 60 yrs

713

714

715

716

717

718

719 **Figure captions**

720 Fig. 1. The geographical distribution of solar flux perturbation.

721

722 Fig. 2. Geographical distributions of the multi-model and annual mean changes in (a-c)
723 precipitation (mm day^{-1}) and (d-f) relative SST (defined as the SST subtracted from the tropical
724 mean SST between 20°S - 20°N , in K), and their zonal-mean profiles over 20°S and 20°N . In the
725 zonal-mean plots, the individual models are color-coded as in Fig. 3 and the multi-model mean is
726 shown in black. Note the differing scale in the zonal-mean precipitation response.

727

728 Fig. 3. The tropical precipitation asymmetry index P_{ASY} (the difference in the precipitation
729 averaged between 0 - 20°N and that between 0 - 20°S normalized by the mean precipitation
730 between 20°S - 20°N), the equatorially symmetric precipitation index P_{SYM} (the average
731 precipitation over 2°S - 2°N divided by that over 20°S - 20°N minus 1), and the area-averaged
732 precipitation between 20°S - 20°N divided by a factor of 20 (in mm day^{-1}). The gray star symbol
733 overlaid with CNTL is the observed value based on Global Precipitation Climatology Project
734 (GPCP) data averaged between 1980 and 1999.

735

736 Fig. 4. Geographical distributions of (a-c) the multi-model and annual mean changes in global
737 surface temperature (in K) and its zonal-mean profile, and (d-f) the multi-model, zonal and
738 annual mean temperature changes (shading; in K) and anomalous meridional streamfunction
739 (contours interval = $3 \times 10^9 \text{ kg s}^{-1}$). Solid (dashed) contour indicates a clockwise
740 (counterclockwise) circulation. In the zonal-mean plots, the individual models are color-coded as
741 in Fig. 3 and the multi-model mean is shown in black.

742

743 Fig. 5. Scatter plot of the precipitation asymmetry index (P_{ASY}) response (unitless) versus (a) the
744 inter-hemispheric difference of sea surface temperature response over 20°S-20°N (in K) and (b)
745 the anomalous cross-equatorial atmospheric energy transport F_{ATM0} (in PW). The individual
746 models are color-coded as in Fig. 3.

747

748 Fig. 6. Schematic diagram of the energy fluxes and ITCZ shift. Minus sign in the colored arrows
749 indicates that the given process compensates the prescribed forcing (acting as a negative
750 feedback) while plus sign indicates that the given process amplifies the prescribed forcing
751 (acting as a positive feedback). Gray bars in the colored arrows in panels b and c denote the
752 model spread from ETIN-MIP. (a) A solar flux reduction in the Southern Hemisphere (black
753 open arrow) is balanced by the upward ocean heat uptake response E_{OCN} (green arrow) and a
754 southward cross-equatorial atmospheric energy transport response F_{ATM0} (red arrow) while the
755 TOA radiation response E_{TOA} may act as either dampener or amplifier of forcing (orange arrow).
756 A southward F_{ATM0} is associated with a northward ITCZ shift. (b) Energy flux and ITCZ
757 response to a solar flux reduction in the southern tropics. The forcing is balanced more by F_{ATM0} ,
758 leading to a large ITCZ shift. (c) Energy flux and ITCZ response to a solar flux reduction in the
759 southern extratropics. The forcing is damped effectively by ocean heat uptake response over the
760 Southern Ocean, accompanying a small F_{ATM0} and a muted ITCZ shift.

761

762 Fig. 7. The fractional compensation (in %) by the atmospheric energy transport (C_{ATM}), the
763 ocean heat uptake (C_{OCN}), and the TOA radiation (C_{TOA}) at the equator. The oceanic

764 compensation accomplished within 30°S-30°N is displayed in red bars. The individual models
765 are color-coded as in Fig. 3.

766

767 Fig. 8. Geographical distributions of the multi-model and annual mean changes in (a-c) net
768 downward surface heat flux E_{OCN} and (d-f) effective net TOA radiation $E_{\text{TOA-S}}$, and their zonal-
769 mean profiles. Both E_{OCN} and $E_{\text{TOA-S}}$ are defined positive downward. In the zonal-mean plots,
770 the individual models are color-coded as in Fig. 3 and the multi-model mean is shown in black.

771

772 Fig. 9. (a-c) The multi-model and annual mean ocean temperature in CNTL (shading; in K) and
773 ocean MOC streamfunction changes (contour interval = 2 Sv). Solid (dashed) contour indicates a
774 clockwise (counterclockwise) circulation. (d-f) The multi-model and annual mean ocean
775 temperature changes (shading; in K) and the ocean MOC streamfunction in CNTL (contour
776 interval = 5 Sv).

777

778 Fig. 10. Zonal and annual mean changes in (a-c) sea ice fraction (in %) and (d-f) low cloud cover
779 (in %), for the selected models where the variables were made available. For both variables, the
780 monthly changes are weighted by the monthly insolation before taking the annual-mean. The
781 individual models are color-coded as in Fig. 3 and the multi-model mean is shown in black.

782

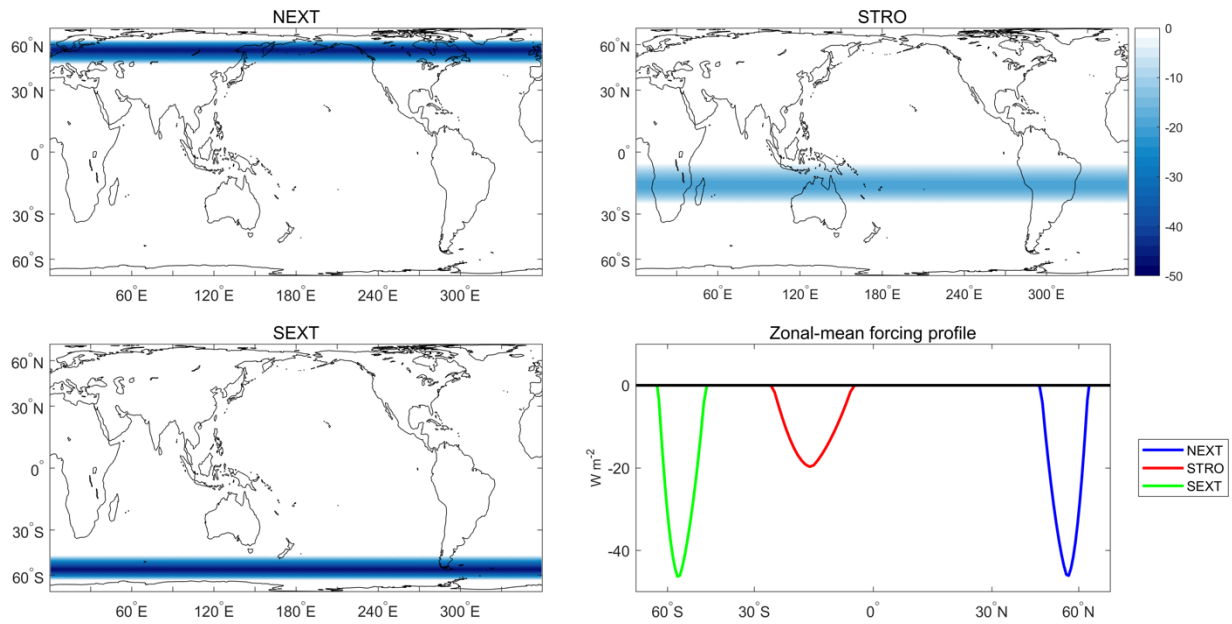
783

784

785

786

787



788

789

790 Fig. 1. The geographical distribution of solar flux perturbation.

791

792

793

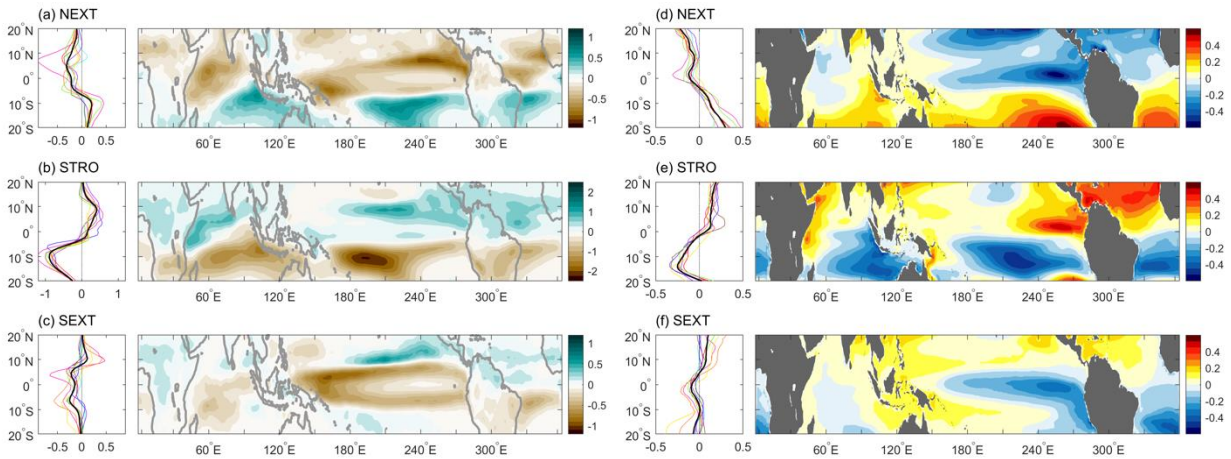
794

795

796

797

798



799

800 Fig. 2. Geographical distributions of the multi-model and annual mean changes in (a-c)
 801 precipitation (mm day^{-1}) and (d-f) relative SST (defined as the SST subtracted from the tropical
 802 mean SST between 20°S - 20°N , in K), and their zonal-mean profiles over 20°S and 20°N . In the
 803 zonal-mean plots, the individual models are color-coded as in Fig. 3 and the multi-model mean is
 804 shown in black. Note the differing scale in the zonal-mean precipitation response.
 805

806

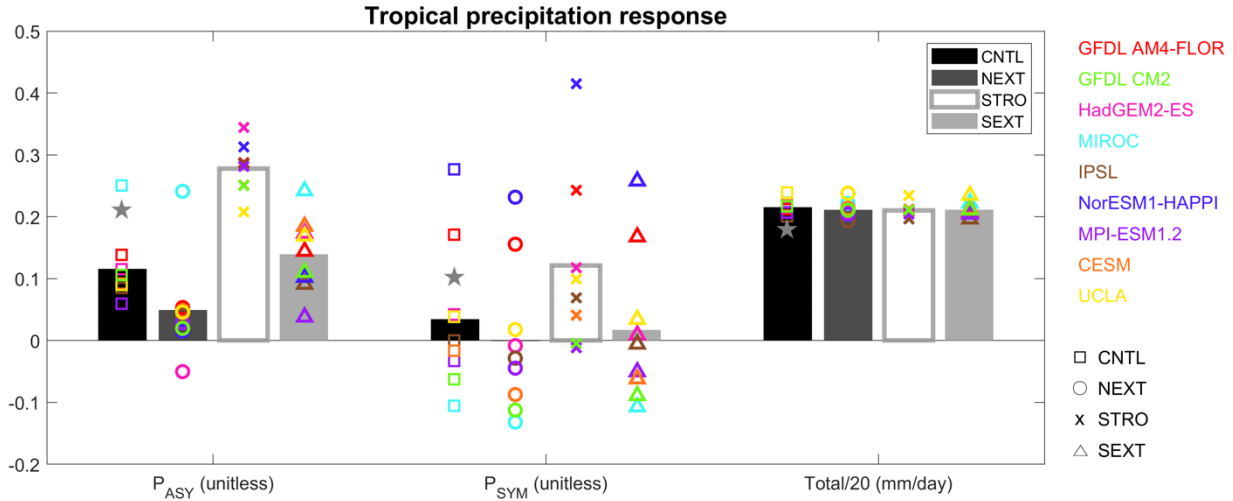
807

808

809

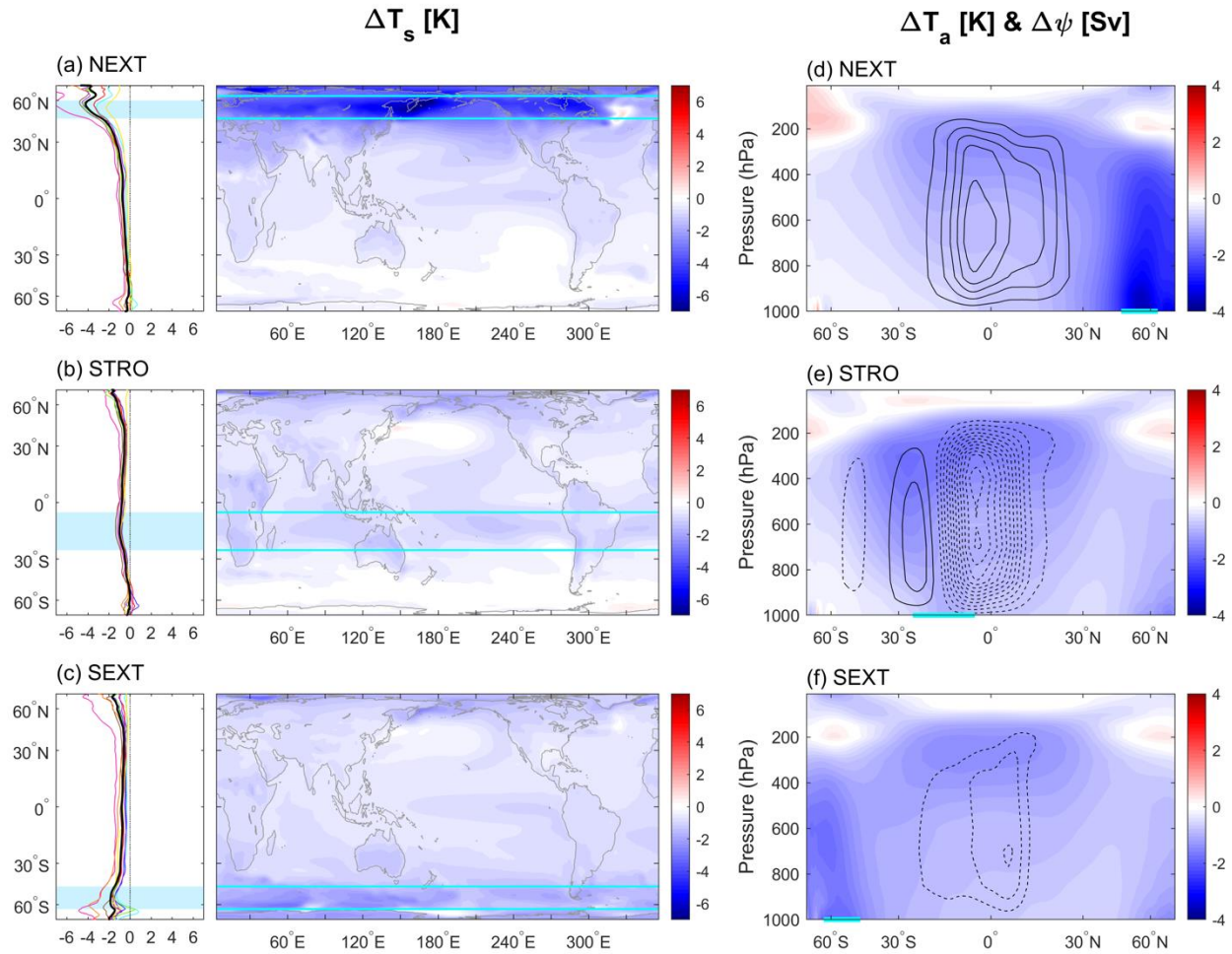
810

811



812

813 Fig. 3. The tropical precipitation asymmetry index P_{ASY} (the difference in the precipitation
 814 averaged between 0-20°N and that between 0-20°S normalized by the mean precipitation
 815 between 20°S-20°N), the equatorial precipitation index P_{SYM} (the average precipitation over 2°S-
 816 2°N divided by that over 20°S-20°N minus 1), and the area-averaged precipitation between
 817 20°S-20°N divided by a factor of 20 (in mm day⁻¹). The gray star symbol overlaid with CNTL is
 818 the observed value based on Global Precipitation Climatology Project (GPCP) data averaged
 819 between 1980 and 1999.



820

821 Fig. 4. Geographical distributions of (a-c) the multi-model and annual mean changes in global
 822 surface temperature (in K) and its zonal-mean profile, and (d-f) the multi-model, zonal and
 823 annual mean temperature changes (shading; in K) and anomalous meridional streamfunction
 824 (contours interval = $3 \times 10^9 \text{ kg s}^{-1}$). Solid (dashed) contour indicates a clockwise
 825 (counterclockwise) circulation. In the zonal-mean plots, the individual models are color-coded as
 826 in Fig. 3 and the multi-model mean is shown in black.

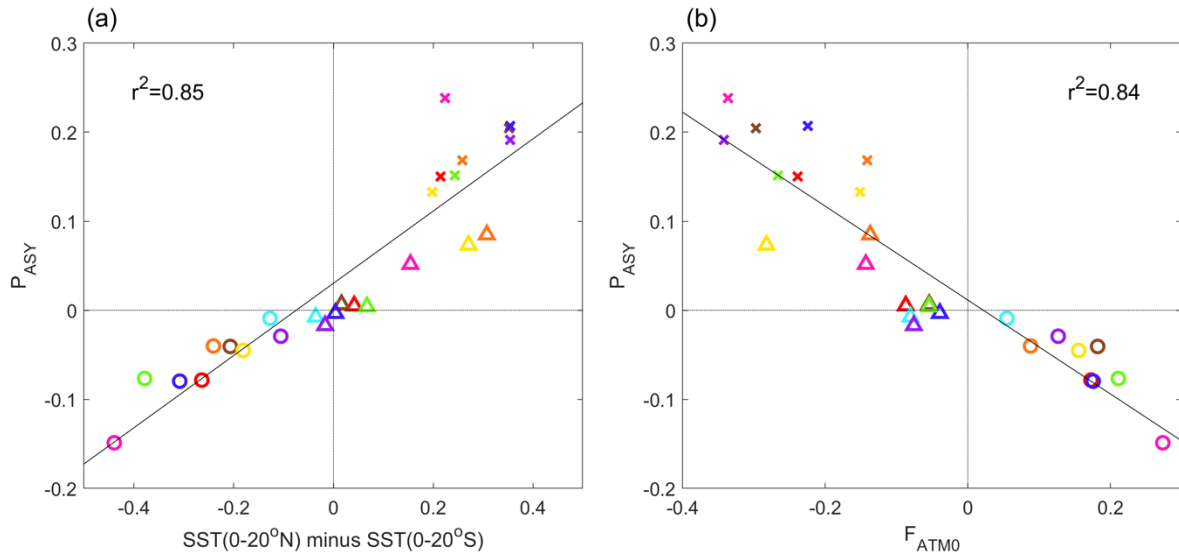
827

828

829

830

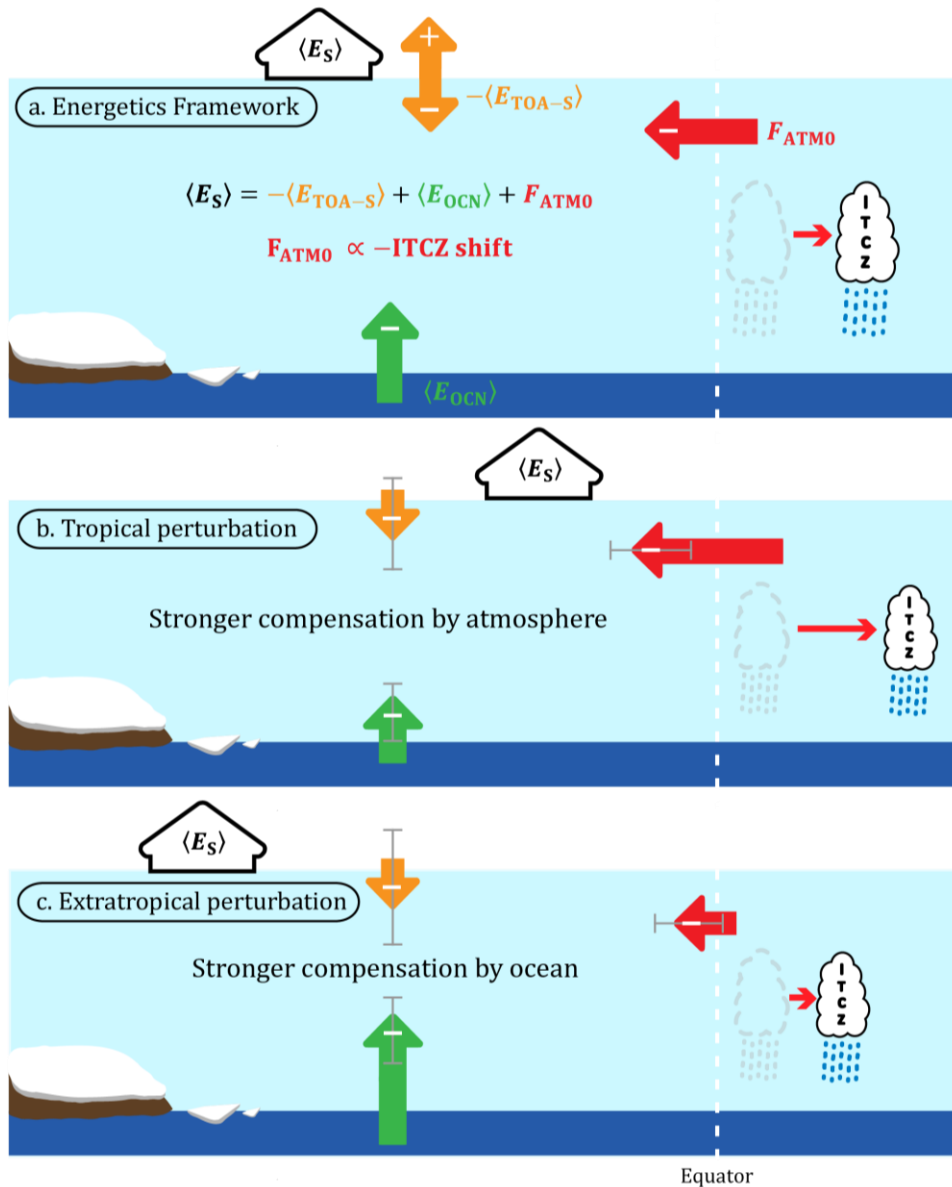
831



832
833
834
835
836
837
838
839

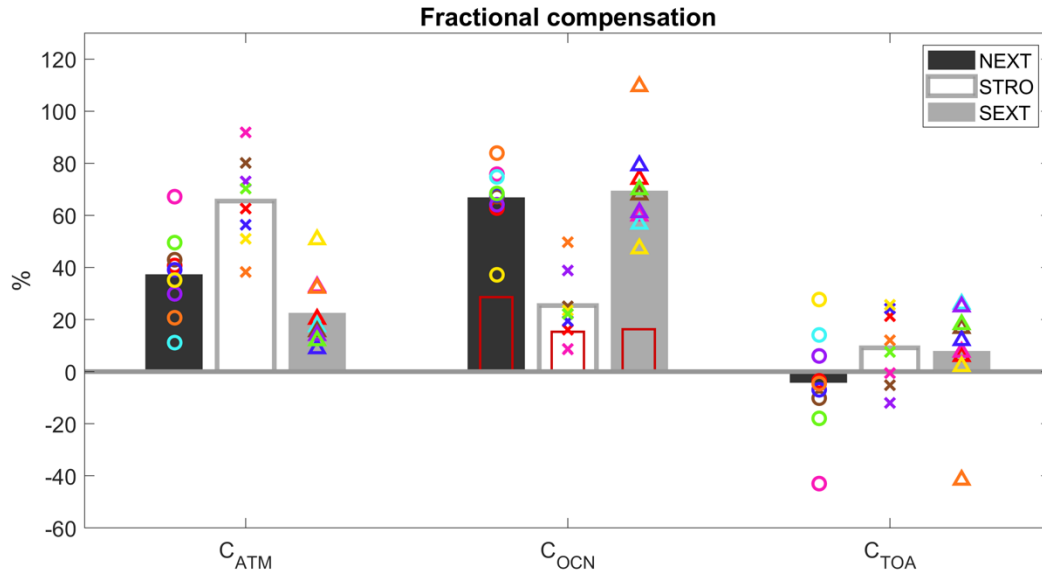
Fig. 5. Scatter plot of the precipitation asymmetry index (P_{ASY}) response (unitless) versus (a) the inter-hemispheric difference of sea surface temperature response over $20^{\circ}S-20^{\circ}N$ (in K) and (b) the anomalous cross-equatorial atmospheric energy transport F_{ATM0} (in PW). The individual models are color-coded as in Fig. 3.

840
841
842
843
844



845

846 Fig. 6. Schematic diagram of the energy fluxes and ITCZ shift. Minus sign in the colored arrows
 847 indicates that the given process compensates the prescribed forcing (acting as a negative
 848 feedback) while plus sign indicates that the given process amplifies the prescribed forcing
 849 (acting as a positive feedback). Gray bars in the colored arrows in panels b and c denote the
 850 model spread from ETIN-MIP. (a) A solar flux reduction in the Southern Hemisphere (black
 851 open arrow) is balanced by the upward ocean heat uptake response E_{OCN} (green arrow) and a
 852 southward cross-equatorial atmospheric energy transport response F_{ATMO} (red arrow) while the
 853 TOA radiation response E_{TOA} may act as either dampener or amplifier of forcing (orange arrow).
 854 A southward F_{ATMO} is associated with a northward ITCZ shift. (b) Energy flux and ITCZ
 855 response to a solar flux reduction in the southern tropics. The forcing is balanced more by F_{ATMO} ,
 856 leading to a large ITCZ shift. (c) Energy flux and ITCZ response to a solar flux reduction in the
 857 southern extratropics. The forcing is damped effectively by ocean heat uptake response over the
 858 Southern Ocean, accompanying a small F_{ATMO} and a muted ITCZ shift.



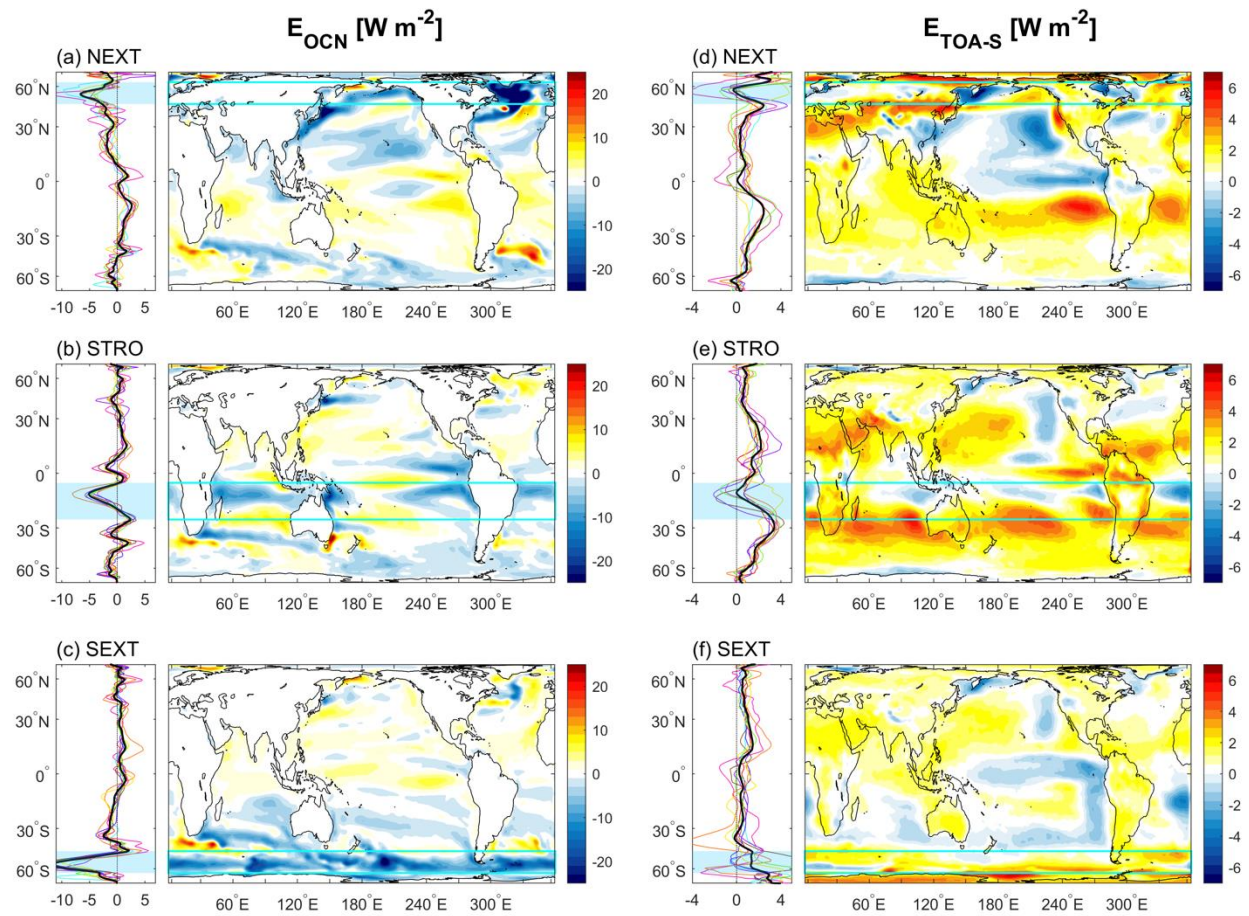
859
 860 Fig. 7. The fractional compensation (in %) by the atmospheric energy transport (C_{ATM}), the
 861 ocean heat uptake (C_{OCN}), and the TOA radiation (C_{TOA}) at the equator. The oceanic
 862 compensation accomplished within 30°S-30°N is displayed in red bars. The individual models
 863 are color-coded as in Fig. 3.

864

865

866

867



868

869 Fig. 8. Geographical distribution of the multi-model and annual mean changes in (a-c) net
 870 downward surface heat flux E_{OCN} and (d-f) effective net TOA radiation E_{TOA-S} and their zonal-
 871 mean profiles. Both E_{OCN} and E_{TOA-S} are defined positive downward. In the zonal-mean plots,
 872 the individual models are color-coded as in Fig. 3 and the multi-model mean is shown in black.
 873

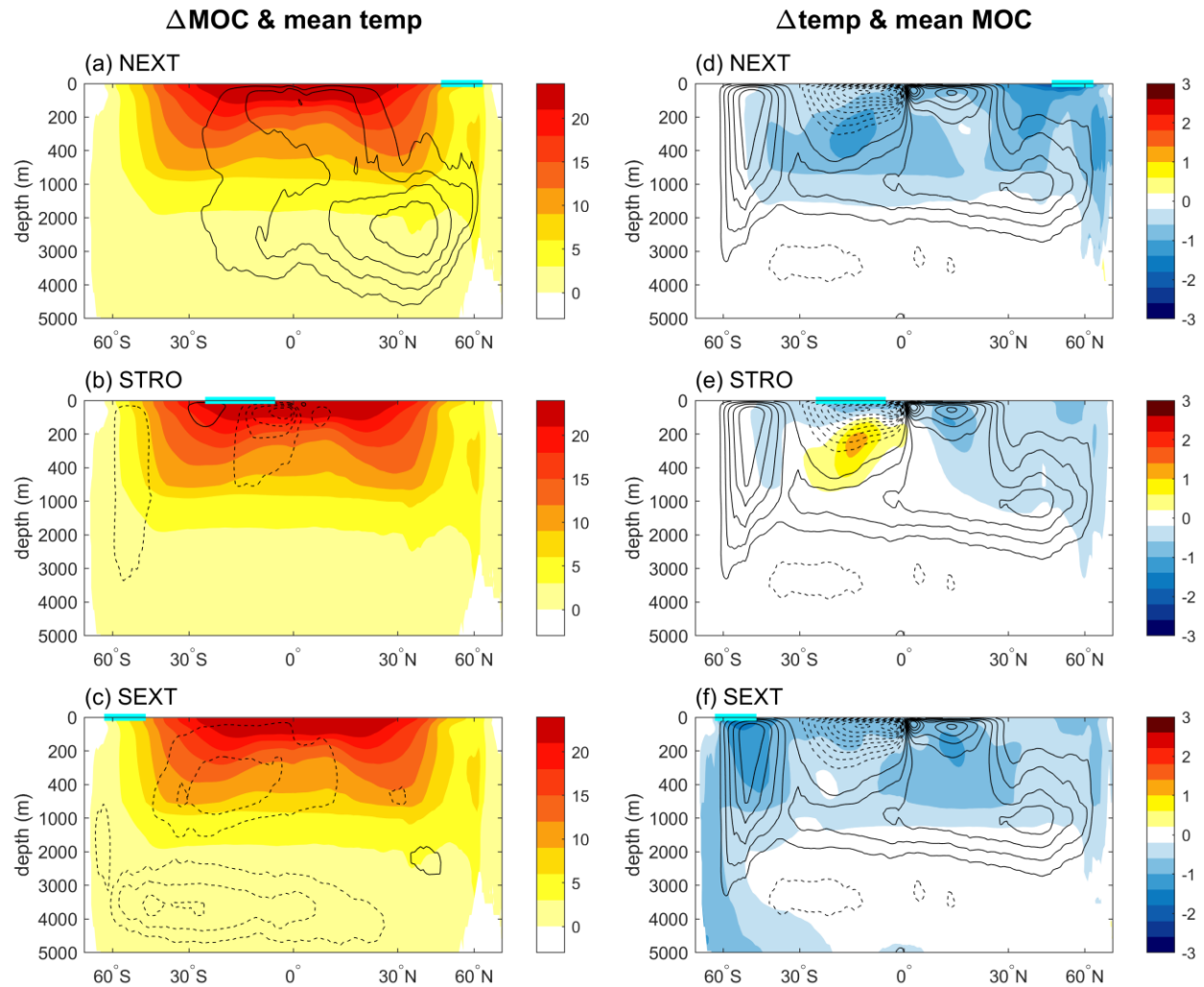
874

875

876

877

878



879

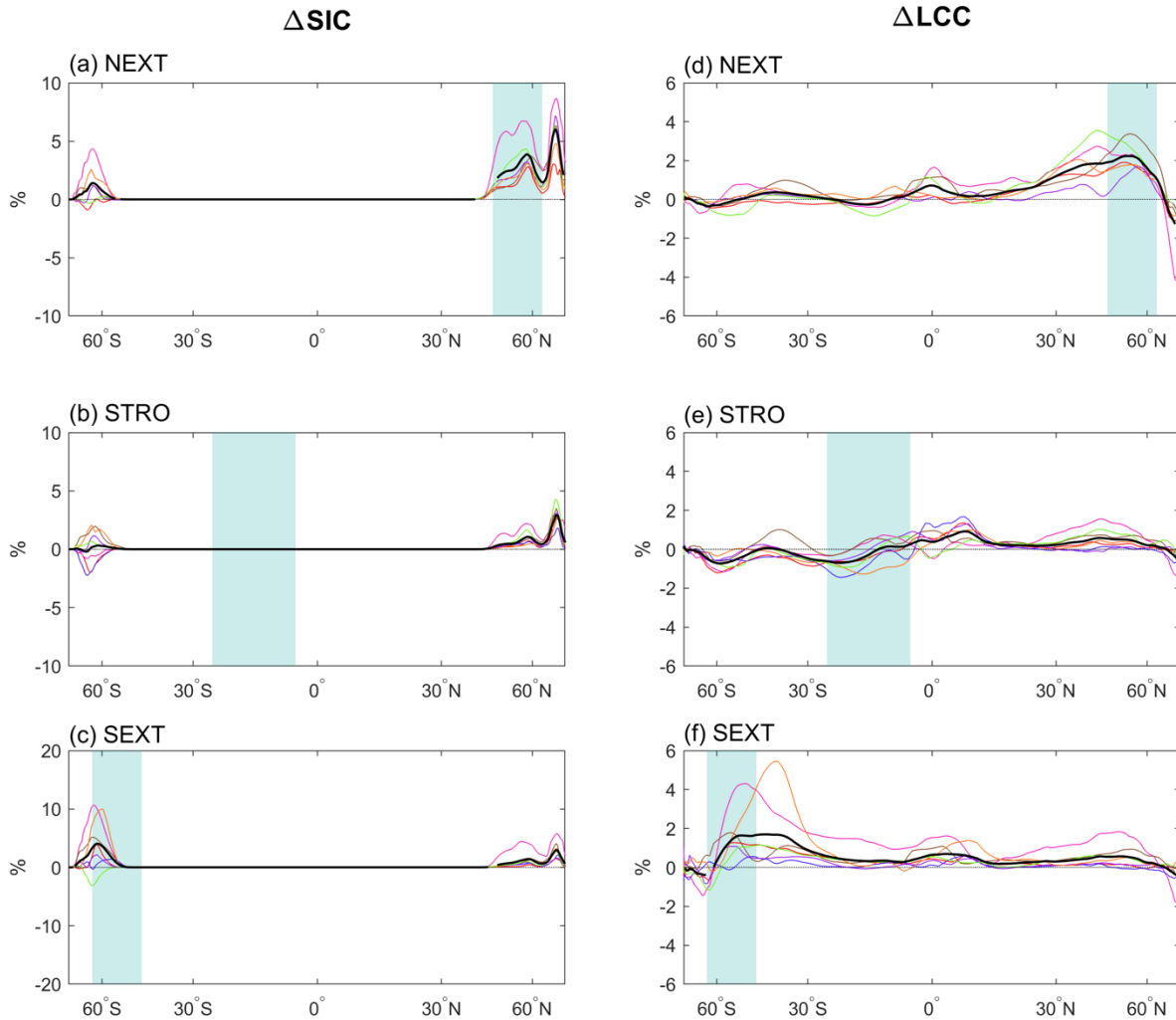
880 Fig. 9. (a-c) The multi-model and annual mean ocean temperature in CNTL (shading; in K) and
 881 ocean MOC streamfunction changes (contour interval = 2 Sv). Solid (dashed) contour indicates a
 882 clockwise (counterclockwise) circulation. (d-f) The multi-model and annual mean ocean
 883 temperature changes (shading; in K) and the ocean MOC streamfunction in CNTL (contour
 884 interval = 5 Sv).

885

886

887

888



889

890 Fig. 10. Zonal and annual mean changes in (a-c) sea ice fraction (in %) and (d-f) low cloud cover
 891 (in %), for the selected models where the variables were made available. For both variables, the
 892 monthly changes are weighted by the monthly insolation before taking the annual-mean. The
 893 individual models are color-coded as in Fig. 3 and the multi-model mean is shown in black.
 894